LASER & PHOTONICS REVIEWS

www.lpr-journal.org

Scalable On-Chip Microdisk Resonator Spectrometer

Chunlei Sun, Zequn Chen, Yuting Ye, Kunhao Lei, Hui Ma, Maoliang Wei, Renjie Tang, Jianghong Wu, Hongtao Lin, and Lan Li**

On-chip micro-spectrometers are sought after with great effort owing to extensive potential applications in mobile optical sensing and imaging. By multiplexing more physical channels, the reconstructive spectrometers based on the spectral-to-spatial mapping technique can improve the spectral range. However, this method is challenging to implement and sustain due to the increase in system complexity and the decrease of dynamic range or spectral resolution. Here, a micro-spectrometer utilizing a single tunable microdisk resonator (MDR) is demonstrated. Such a single MDR spectrometer has only one physical channel to receive all spectral components with a compact size, overcoming the trade-off among spectral resolution, spectral range, and dynamic range. Leveraging the wavelength and temperature-dependent response matrix, unknown spectra are reconstructed from their corresponding output light intensity vector. The fabricated device illustrates a high resolution of 0.01 nm for a dual peak and a medium resolution of 0.2 nm in the 20 nm spectral range. A wide variety of complex input spectra, including narrowband and broadband spectral signals, can be well recovered, exhibiting the robustness of the spectral reconstruction approach. Moreover, this proposed spectrometer exhibits ease of scalability and flexible configuration to a spectrometer array covering a set of desired and even discrete spectral ranges.

1. Introduction

Miniaturized spectrometers, free from mechanical moving parts, are promising for low-cost, portable sensing, and imaging applications owing to their reduced footprints and weight.[1] The micro-spectrometers sharing the same ideas with the benchtop counterparts, such as dispersive optics and Fourier transforms interferometers, have degraded resolving power since the spectral resolution scales inversely with its footprint.[2–12] In recent years, reconstructive micro-spectrometers based on computational algorithms exploring spectral-to-spatial mapping have been extensively investigated due to superior performances of the spectral resolution and operation bandwidth.[13–21] Diverse integrated photonic structures, such as random scattering media,[16–19] evanescently coupled multimode spiral waveguide,[20] and linear coherent integrated networks[21] are utilized to design a reconstructive micro-spectrometer. Significantly, nanophotonic structures can enhance light–matter interaction, increasing the optical path length, so these spectrometers have a compact size and great spectral resolution.[22] However, the spectral-to-spatial technique for large-scale mapping by splitting input light into many physical detection channels often faces many dilemmas. To name a few, since each channel requires a photodetector, the device footprint and system complexity increase linearly with the number of physical channels. Furthermore, high loss in a strongly scattering medium will be induced as the device footprint increases. The reconstruction error will be affected by the power of each channel and the signal-to-noise ratio (SNR) of each corresponding photodetector. The detection channels with low power will lead to a low dynamic range in the reconstructed spectrum, especially for the high-resolution micro-spectrometer. In addition, scalability, which can further improve spectral range by combining a wavelength demultiplexer without affecting other performance parameters,[23] is also very significant. Simple device structure and broadband spectrum response are highly desired.

Recently, reconstructive spectrometers based on tunable filters or photodetectors using only one or a few physical channels have been reported.[24,25] By tuning the resonance wavelength of the nanobeam cavity filter, different spectral components of incoming light are captured. The reconstruction algorithms are used to

C. Sun, Z. Chen, Y. Ye, R. Tang, J. Wu, L. Li
Key Laboratory of 3D Micro/Nano Fabrication and Characterization of Zhejiang Province
School of Engineering
Westlake University
Hangzhou 310030, China
E-mail: sunchunlei@westlake.edu.cn; lilan@westlake.edu.cn

C. Sun, Z. Chen, Y. Ye, R. Tang, J. Wu, L. Li
Institute of Advanced Technology
Westlake Institute for Advanced Study
Hangzhou 310024, China

K. Lei, H. Ma, M. Wei, H. Lin
Key Laboratory of Micro-Nano Electronics and Smart System of Zhejiang Province
College of Information Science and Electronic Engineering
Zhejiang University
Hangzhou 310027, China

K. Lei, H. Ma, M. Wei, H. Lin
State Key Laboratory of Modern Optical Instrumentation
Zhejiang University
Hangzhou 310027, China

The ORCID identification number(s) for the author(s) of this article can be found under https://doi.org/10.1002/lpor.202200792

DOI: 10.1002/lpor.202200792

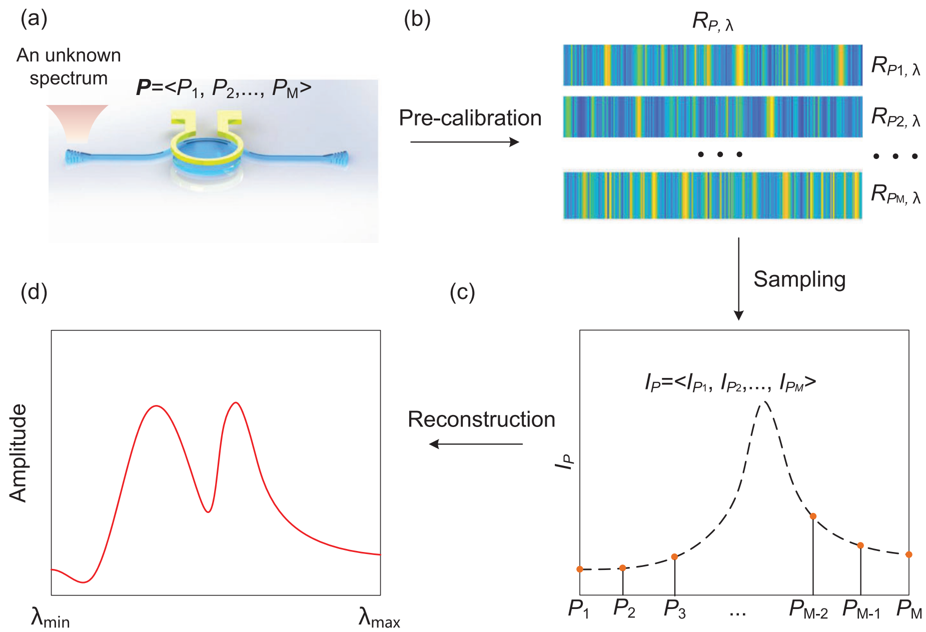

Figure 1. Operation scheme of the MDR spectrometer. a) The spectral response of MDR can be tuned by the driving power applied to the heater. b) The responsivity matrix $R_{P,\lambda}$ depends on the driving power P and the incident light wavelength λ. Each element of the array corresponds to a color in the barcode image. c) The photocurrent in the photodetector is sampled as a function of the driving power P. The sampling process generates the photocurrent vector I_P. d) Reconstruction of the unknown spectra using the $R_{P,\lambda}$ and I_P.

break the 3-dB bandwidth limit of narrowband filters. However, the high spectral resolution requires exact and dense wavelength tuning owing to the low cross-correlation of the transmission spectra of the filters at different driving power. In other words, compared to low cross-correlation response spectra, more samplings or tuning states are necessary for high cross-correlation response spectra, increasing the total driving energy, sampling and reconstruction time. Moreover, the high spectral resolution is often at the cost of a low dynamic range since only one spectral line can be detected once.

In this paper, we report a new scheme for scalable reconstructive micro-spectrometers using a single tunable microdisk resonator (MDR). Unlike other cavity resonators (e.g., microring resonator (MRR),[26] Fabry–Pérot (F–P) cavity[27] and nanobeam cavity[24]) usually operating in a single-mode waveguide, the disk resonator supports hundreds of whispering-gallery modes (WGMs) and typically has a fast and random response spectrum in broad waveband. Due to the smaller scattering loss introduced by sidewall roughness from only one etched sidewall, the high-Q resonator can be obtained, enhancing the optical path length (OPL) difference between different WGMs. The interference of WGMs with different OPL or phase delay produces wavelength and temperature-sensitive output intensity patterns. By tuning the disk resonator using a microheater, different OPL changes for WGMs are generated. One can obtain low cross-correlation of the transmission spectra for different driving power as different WGMs have different temperature sensitivity. Since all the spectral components are received by only one photodetector, the proposed micro-spectrometer overcomes the trade-off among spectral resolution, spectral range, and dynamic range.

2. Results

2.1. Operation Principle

The operation scheme of our proposed MDR spectrometer is displayed in **Figure 1**. It consists of three procedures: 1) pre-calibration, 2) sampling, and 3) reconstruction. The spectral transmission response of the MDR can be tuned by external driving power (P) applied to the microheater in Figure 1a. The continuous responsivity function can be discretized into a matrix $R_{P,\lambda}$ in Figure 1b, which depends on the driving power P and the incident light wavelength λ. Each element of the array corresponds to a color in the optical transmission barcode image. By measuring the spectral responses at each driving power P_i using a known tunable laser source, the responsivity row vector $R_{Pi,\lambda}$ in spectral response matrix $R_{P,\lambda}$ can be pre-calibrated. Completing all sampling generates the full response matrix $R_{P,\lambda}$. The photocurrent response to the unknown spectrum of the incident light will be sampled at M different driving power (P_1 to P_M) to generate the output light intensity vector I_P in Figure 1c. Based on the response matrix $R_{P,\lambda}$ generated by the pre-calibration procedure and the response vector I_P measured in the sampling procedure, the spectrum of arbitrary incident light can be reconstructed, as shown in Figure 1d.

2.2. Device Design

The micro-spectrometer studied in this work is formed of a tunable MDR coupled to a bent waveguide, as demonstrated in **Figure 2**a. The inset shows the structure with radius R, coupling gap G, and coupling wrap angle θ. MDR is a fundamental

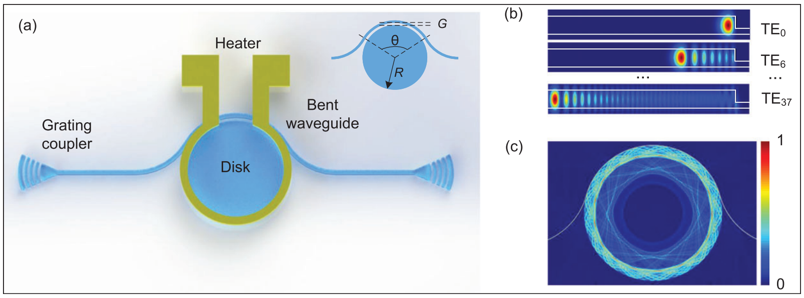

Figure 2. Design and simulation of the MDR. a) Schematic of the proposed tunable MDR. The inset shows the structure with radius R, coupling gap G, and coupling wrap angle θ. b) WGMs in the MDR with a radius of 60 µm. The white lines indicate the profile of the MDR. c) Simulated electric field distribution in the MDR by 2D FDTD.

component in the photonic system with extensive applications in chemical and biological sensing,[28] ultra-small laser,[29] and optical communication[30] due to its typically high Q-factors across a wide wavelength range. Compared to the MRR, the MDR have a much higher Q-factor owing to only one etched sidewall, resulting in much lower scattering loss. Besides, there supports massive WGMs in the MDR because of the single-side light field constraint. For example, in a silicon MDR with a radius of 60 µm, hundreds of WGMs can be supported. The comparison between MRR and MDR for spectrum analysis will be given in the Section 3. Figure 2b shows a few WGMs of traverse-electrical (TE) polarization in the MDR. The key to achieving a high-resolution and large-spectral-range spectrometer is to make the response spectra of the MDR vary fast and randomly. Thus, the MDR spectrometer is preferred to work under high Q-factor and multiple WGM operation conditions. Intuitively, the MDR with a high Q-factor can enhance the OPL difference between different WGMs. For most previous applications, a single-mode operation to avoid exciting multiple WGMs over the entire free spectral range (FSR) is desired. Therefore, one needs to elaborately design the coupling gap and coupling wrap angle of the MDR to achieve phase matching between the fundamental WGM and the waveguide mode. Here, more WGMs in the MDR are required, enlarging the difference between the shortest and longest optical paths. Interference of different WGMs produces output intensity patterns that are sensitive to wavelength and temperature changes. The microheater provides a non-uniform thermal field distribution on the MDR, producing very different impacts on WGMs with different orders. Thus different optical path delays are introduced, resulting in random spectral responses. By tuning the MDR with low power consumption, the response spectrum of the MDR can vary dramatically. Therefore, minor wavelength spacing can also be distinguished. Figure 2c shows multiple WGMs in the MDR by 2D finite difference time domain (2D FDTD) simulation. To excite more WGMs, an MDR with $R = 100$ µm, $\theta = 150°$ and $G = 150$ nm is adopted.

2.3. Device Characterization

Figure 3a,b shows the microscope images of the tunable MDR. Figure 3c illustrates the normalized measured response matrix $R_{P,\lambda}$. The insertion loss in the 1500–1600 nm range is <1.5 dB. The driving power range is 0 to 160 mW with a sampling interval of 2.5 mW. $R_{P,\lambda}$ was pre-calibrated with a tunable laser (Santec full-band TSL, 1260–1630 nm) with a wavelength scanning step of 1 pm. Actually, the bandwidth where the proposed MDR has a fast and random response spectrum is now limited only by the single-mode condition of the waveguide. For clarity, only the wavelength range of 1500–1510 nm is demonstrated. Note that the high linearity of the MDR spectrometer is important, which means that the spectrometer can work at different input power for only one pre-calibration. The analysis of the linearity of the MDR spectrometer is given in Section S1, Supporting Information. The autocorrelation function can evaluate how fast and randomly the spectrum varies. The formula of the correlation function is given in ref. [20] and $\Delta\lambda$ in Figure 3d,e refers to the wavelength lag between the response spectra. The full width at half maximum (FWHM) of the autocorrelation function of the MDR with 100 and 200 µm radius is 11.2 and 6.5 pm, respectively, which provides an estimate for the spectral resolution. Since the MDR with a 200 µm radius has a higher Q-factor and more WGMs than that with a 100 µm radius, the spectral resolution is higher. We also calculated the cross-correlation functions between the measured spectra with 0 mW and other power, as shown in Figure 3e. The cross-correlation function can characterize the similarity between the response spectra at different wavelengths. A value smaller than 0.5 indicates a moderate or weak correlation between the response spectra for different power. By picking the maximum of each cross-correlation function, we can obtain the change rule between the maximum cross-correlation value and the driving power, as shown in Figure 3f. The maximum cross-correlation value decreases as the driving power increases, and the maximum cross-correlation value of the MDR with a 100 and 200 µm radius decreases at almost the same speed. Considering the MDR with a 200 µm radius has a much larger size than that with a 100 µm radius, the heating temperature at the waveguide surface is lower. Thus, the cross-correlation function of the MDR with a 200 µm radius is more sensitive to the temperature change. Therefore, we can obtain a random and high-orthogonality response matrix through low power consumption.

2.4. Spectrum Reconstruction

The spectral response matrix $R_{P,\lambda}$ can be extracted from the pre-calibration process, as shown in Figure 3c. The output light

LASER & PHOTONICS REVIEWS
www.lpr-journal.org

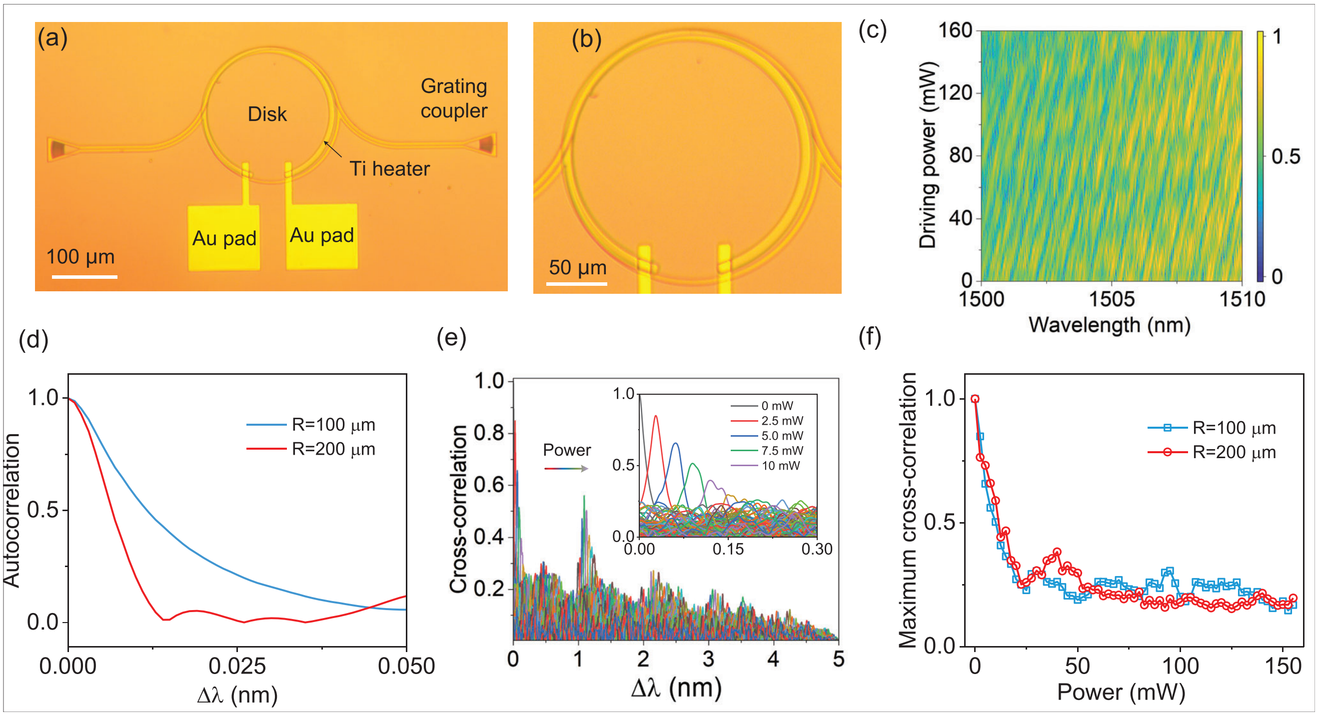

Figure 3. a) Microscope image of the tunable MDR. b) Zoom-in view of the MDR. c) Normalized measured response matrix $R_{P,\lambda}$. The driving power range is 0 to 160 mW with a sampling interval of 2.5 mW. d) Autocorrelation functions of the measured spectra of the MDR with a radius of 100 and 200 μm. e) Cross-correlation functions between the measured spectra with 0 mW and other power. The inset shows the enlarged image. f) Maximum cross-correlation values between the measured spectra with 0 mW and other power.

intensity at different driving power I_P is synthesized for any input spectrum by adding up the output power of each wavelength. Thus, the I_P related to the input spectrum S_λ by

$$I_P = R_{P,\lambda} \times S_\lambda \tag{1}$$

Generally, the dimension of the input spectrum N is much larger than the sampling times M. It is a well-known underdetermined linear algebra problem, which can be solved by minimizing l_2 norm using a linear regression algorithm (LSM). To increase the reconstruction performance, regularization of the l_2 norm is usually added to the regression with a certain weight coefficient α:

$$Minimize\left|\left|I_P - R_{P,\lambda} \times S_\lambda\right|\right|^2 + \alpha\left|\left|S_\lambda\right|\right|^2 \ subject\ to\ 0 \le S_\lambda \le 1 \tag{2}$$

The weight coefficient α is estimated from a cross-validation analysis.[13] Here the sampling resolution of $R_{P,\lambda}$ is 1 pm, which is much smaller than the spectral resolution of the MDR spectrometer. Direct spectrum reconstruction by Equation (2) limits the spectral range. We adopt the compressive sensing algorithm to reconstruct spectra to increase the spectral range.[20,24,31] Alternatively, we choose Gaussian function fitting to discretize the input spectrum:

$$S_{N\times1} = \Phi_{N\times K}\, t_{K\times1} \tag{3}$$

where $t_{K\times1}$ is the weighting coefficient vector, and K is the spectral channel number. $\Phi_{N\times K}$ is the basis matrix whose columns are all Gaussian functions. Equation (2) can be rewritten as:

$$Minimize\left|\left|I - \sqrt{\ } \cdot t\right|\right|^2 + \alpha\left|\left|t\right|\right|^2 \ subject\ to\ 0 \le t \le 1 \tag{4}$$

where $\Theta_{M\times K} = R_{M\times N}\,\Phi_{N\times K}$. Through the compressive sensing algorithm, the dimension of the unknown input spectrum to be solved is compressed from N to K (K<<N).

The autocorrelation function of the response matrix can only estimate the spectral resolution. In contrast, the actual spectral resolution of the MDR spectrometer depends on the minimum wavelength spacing that the spectrometer can distinguish. **Figure** 4a shows the good reconstruction of a spectrum with dual peaks, and the peak distance is 0.01 nm. To decrease the reconstruction error, the Gaussian functions with the 3-dB bandwidth of 0.01 nm are adopted in the range of 1505.2–1505.5 nm, and the spectral channel number K is equal to 65. By choosing a moderate resolution, the spectral range can be improved. The resolution can be tuned by the spectral channel number K and 3-dB bandwidth of Gaussian functions. To verify the robustness of the MDR spectrometer, we recover a broadband spectrum with sharp roll-off edges with high fidelity in the range of 1503–1507 nm, as shown in Figure 4b. In Figure 4c, we recover a spectrum consisting of a sharp line with a linewidth of 0.5 nm on top of a broad peak. By choosing the Gaussian functions with the 3-dB bandwidth of 0.5 nm, the spectral range can increase to 20 nm. Due to the high-Q multiple-WGM operation across a wide wavelength range, the spectral range of the MDR spectrometer can be increased further.

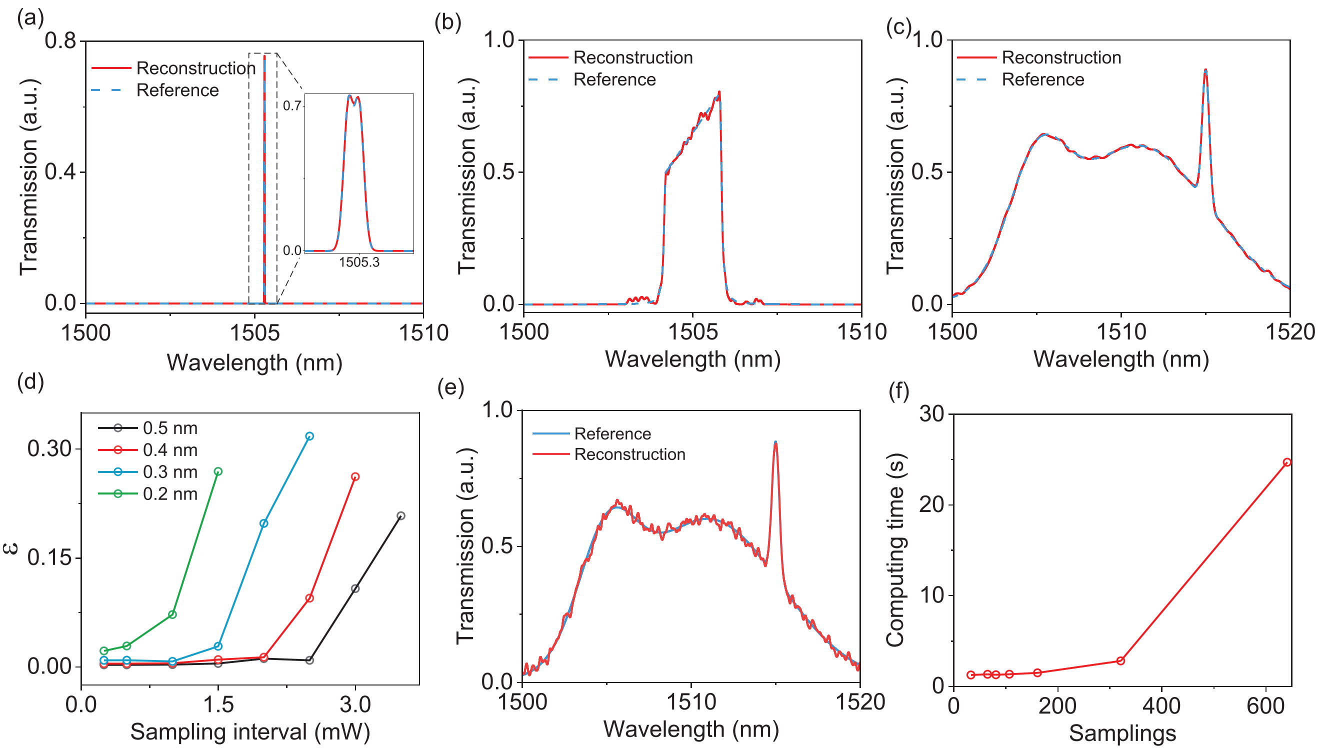

Figure 4. Reconstructing various types of spectra. a) Dual peak with 0.01 nm distance. b) Broadband spectrum with sharp roll-off edges. c) Broad spectrum with a bandwidth of 20 nm and a sharp peak. d) Relative reconstruction error as a function of the number of samplings. The sampling interval is 0.25, 0.5, 1, 1.5, 2, 2.5, 3, and 5 mW (641, 321, 161, 108, 81, 65, 54, and 33 samplings). The legend refers to the spectral resolution. The effective spectral channel is defined as the quotient of the spectral range divided by the spectral resolution. e) Reconstructed spectrum using 321 samplings with spectral resolution of 0.2 nm and spectral range of 20 nm. The input spectrum is the same with that used in Figure 4c. f) Computing time as a function of samplings.

To study the relationship between the sampling interval and relative reconstruction error, the spectrum in Figure 4c of the manuscript is used to test. The relative reconstruction error was defined as[21]

$$\varepsilon = \frac{\left[\sum_{i=1}^{N} \left(S - S_0\right)^2\right]^{\frac{1}{2}}}{\left(\sum_{i=1}^{N} S_0{}^2\right)^{\frac{1}{2}}} \tag{5}$$

where S is the reconstructed spectrum and S_0 is the original spectrum, N is the number of wavelength channels. The error ε is between 0 and 1. The driving power range is 0–160 mW with a sampling interval of 0.25, 0.5, 1, 1.5, 2, 2.5, 3, and 5 mW (641, 321, 161, 108, 81, 65, 54, and 33 samplings). We calculated the relative reconstruction error for different sampling intervals, as shown in Figure 4d. The relative reconstruction error increases with the sampling interval for the same spectral resolution. However, the relative reconstruction error improvement becomes unobvious when the sampling interval is smaller than a certain value. It can be attributed that the orthogonality of two adjacent samplings decreases as the sampling interval decreases. Thus, increasing the samplings in the same driving power range cannot always improve the reconstruction performance. Figure 4e shows the reconstructed spectrum with a tolerable reconstruction error of 0.029 using 321 samplings. The spectral resolution is 0.2 nm, and the spectral range is 20 nm. We also obtained the computing time for different samplings, as shown in Figure 4f. The optimization algorithm was implemented in MATLAB software on a desktop computer with 4-core processors and 16 GB RAM. Clearly, the computing time shows an almost exponential function as an increasing number of samplings.

3. Discussions

Leveraging the high-Q and multiple-WGM features of the MDR, the proposed micro-spectrometer can realize narrowband and broadband spectrum analysis. Compared to the tunable MRR, the response spectrum of the MDR is faster and more random, resulting in lower cross-correlation functions between different driving power. Therefore, the MDR spectrometer performs better for spectrum reconstruction than the MRR spectrometer. A detailed comparison is given in Section S2, Supporting Information. It is always tried and true to deliver better performance in terms of spectral resolution and spectral range using simply more samplings (smaller sampling interval). However, the cross-correlation of response functions for two adjacent samplings decreases as the number of samplings, which cannot improve the performance indefinitely. Increasing the driving power or etching thermal isolation trenches around the MDR can dramatically enhance the heating temperature of the MDR.[10,32] Another method is to increase the intraluminal modes or to optimize the

Table 1. Comparison of reconstructive micro-spectrometers..

Spectrometer	Resolution	Spectral range	Physical channel	Passive or active	Footprint
Disordered photonic chip[17]	0.75 nm	25 nm	25	Passive	50 µm × 25 µm
Disordered photonic chip[18]	0.25 nm	30 nm (sparse spectrum)	8	Passive	30 µm × 12.8 µm
Stratified waveguide filters[19]	0.45 nm	180 nm (sparse spectrum)	32	Passive	35 µm × 260 µm
Multimode spiral waveguide[20]	0.01 nm	2 nm (sparse spectrum)	40	Passive	500 µm × 500 µm
Coherent network[21]	0.02 nm	12 nm (sparse spectrum)	64	Passive	520 µm × 220 µm
Cascaded nanobeam cavities[24]	0.32 nm	16 nm	3	Active	18 µm × 18 µm
Microdisk (This work)	0.01 nm 0.2 nm	0.3 nm 20 nm	1	Active	200 µm × 200 µm

heater layout to make the response function of the MDR spectrometer more sensitive to temperature change. Thus, we can get more response spectra with low cross-correlation, improving the spectral range or resolution. In addition, whether the high-resolution feature can be kept when the MDR spectrometer operates in a wide spectral range depends on the input spectrum type. For an unknown general spectrum, it is difficult to be reconstructed with low error since the spectral channel number K is much larger than the sampling number. The recovered spectrum may be collapsed for the under-sampling case. For a sparse spectrum meaning that K is smaller than the sampling number, the high-resolution feature can be attained in a wide spectral range with low reconstruction error. Typically, the smaller K is, the lower the error.

On the other hand, like most integrated photonic devices based on resonance cavities, the MDR spectrometer is sensitive to temperature change since the response matrix could be altered. The temperature sensitivity depends on the FWHM of the autocorrelation: the smaller the FWHM of the autocorrelation is, the more sensitive the MDR is to temperature change. The existing commercial thermo-electric cooler (TEC) temperature control console can provide temperature stabilization of 0.01 °C for the environment temperature from −7 to 61 °C. In addition, the MDR is an inherent temperature sensor.[33] The temperature change can be detected, thus, offsetting the wavelength shift of the reconstructed spectra to avoid recalibrating the response matrix (see Section S3, Supporting Information).

Table 1 shows a comparison of the reported integrated reconstructive micro-spectrometers in recent years. Compared to previously reported reconstructive schemes, our demonstrated MDR spectrometer can not only analyze special sparse spectra but also various general spectra with both high resolution and broad spectral range using only one physical channel. To further enhance the spectral range without degrading other merits, such as spectral resolution and dynamic range, a promising method is to introduce wavelength division multiplexing (WDM) technology.[23] Due to the simple device structure and broadband spectrum response of the MDR, our proposed spectrometer is easily scalable to achieve parallelism in the spectrometer system. Thus, the combined bandwidth can be significantly increased by parallelly implementing a spectrometer array covering a set of target spectral ranges.

4. Conclusion

In this study, we reported an on-chip spectrum analysis method with a high-resolution and large dynamic range through a simple configuration. The proposed micro-spectrometer with a single tunable MDR can generate fast and random response spectra. The cross-correlation function peak vanishes fast as the driving power, constructing a random and high-orthogonality response matrix with low driving power. The MDR spectrometer exhibits an insertion loss of <1.5 dB across a wide wavelength range and a resolution of 0.01 nm for a dual peak around 1505 nm. The spectral range can be increased to 20 nm by adopting a moderate resolution of 0.2 nm. Adopting thermal isolation trenches around the MDR or parallelism in a spectrometer array by WDM technology can efficiently improve the spectral range. Various complex spectra containing narrowband and broadband spectral components can be well recovered, demonstrating the large robustness of spectrum reconstruction. In addition, the proposed micro-spectrometer overcomes the trade-off between dynamic range and spectral resolution. Such a scalable micro-spectrometer achieves high resolution, high dynamic range, and low loss in a compact footprint, which is expected to impact mobile sensing in the lab-on-chip system significantly.

5. Experimental Section

Using electron-beam lithography (EBL, Raith Voyager) and subsequent inductively coupled plasma (ICP, Samco) processes, the MDR spectrometer was fabricated on a 220-nm silicon-on-insulator (SOI) platform. The rib waveguides were fabricated by partial etching with a depth of 150 nm to achieve a high coupling ratio. Then, a layer of silica-thin film with a thickness of 800 nm was deposited by plasma-enhanced chemical vapor deposition (PECVD) to cover the whole device. Titanium, chromium, and gold with different thicknesses were patterned by ultraviolet lithography and deposited by electron beam evaporation to achieve a thermo-optical heater (100 nm Ti/10 nm Au) and contact pads (5 nm Cr/100 nm Au). The width of the titanium heater was 7 µm. At the same time, a layer of SU-8 with a thickness of 500 nm was deposited on the equipment to prevent further oxidation of the titanium heater. The contact pad windows were opened to connect the electric probe and the driving circuit of the micro-heater.

Supporting Information

Supporting Information is available from the Wiley Online Library or from the author.

Acknowledgements

The authors thank Westlake Center for Micro/Nano Fabrication, Instrumentation and Service Center for Physical Sciences at Westlake University, and ZJU Micro-Nano Fabrication Center at Zhejiang University for the facility support. The authors thank Qing Zhao for providing the technical support for dry etching. Funding was provided by National Key Research and Development Program of China (2019YFB2203003); National Natural Science Foundation of China (62175202, 12104375, 61975179, 91950204); Zhejiang Provincial Natural Science Foundation of China (LD22F040002); and Leading Innovative and Entrepreneur Team Introduction Program of Zhejiang (2020R01005).

Conflict of Interest

The authors declare no conflict of interest.

Data Availability Statement

The data that support the findings of this study are available from the corresponding author upon reasonable request.

Keywords

integrated optics devices, optical filters, spectrometers

Received: October 19, 2022
Revised: December 4, 2022
Published online:

[1] D. M. Kita, B. Miranda, D. Favela, D. Bono, J. Michon, H. Lin, T. Gu, J. Hu, *Nat. Commun.* **2018**, *9*, 4405.
[2] G. Calafiore, A. Koshelev, S. Dhuey, A. Goltsov, P. Sasorov, S. Babin, V. Yankov, S. Cabrini, C. Peroz, *Light: Sci. Appl.* **2014**, *3*, e203.
[3] M. Faraji-Dana, E. Arbabi, A. Arbabi, S. M. Kamali, H. Kwon, A. Faraon, *Nat. Commun.* **2018**, *9*, 4196.
[4] S.-H. Oh, K.-D. Ahn, H.-y. Choi, *Microelectron. Eng.* **2019**, *217*, 111130.
[5] B. B. C. Kyotoku, L. Chen, M. Lipson, *Opt. Express* **2010**, *18*, 102.
[6] A. Li, J. Davis, A. Grieco, N. Alshamrani, Y. Fainman, *Photonics Res.* **2020**, *8*, 219.
[7] R. Cheng, C.-L. Zou, X. Guo, S. Wang, X. Han, H. X. Tang, *Nat. Commun.* **2019**, *10*, 4104.
[8] A. Li, Y. Fainman, *Laser Photonics Rev.* **2021**, *15*, 2000358.
[9] M. C. Souza, A. Grieco, N. C. Frateschi, Y. Fainman, *Nat. Commun.* **2018**, *9*, 665.
[10] S. N. Zheng, J. Zou, H. Cai, J. F. Song, L. K. Chin, P. Y. Liu, Z. P. Lin, D. L. Kwong, A. Q. Liu, *Nat. Commun.* **2019**, *10*, 2349.
[11] D. Pohl, M. Reig Escalé, M. Madi, F. Kaufmann, P. Brotzer, A. Sergeyev, B. Guldimann, P. Giaccari, E. Alberti, U. Meier, R. Grange, *Nat. Photonics* **2020**, *14*, 24.
[12] L. Zhang, J. Chen, C. Ma, W. Li, Z. Qi, N. Xue, *Laser Photonics Rev.* **2021**, *15*, 2100016.
[13] Z. Yang, T. Albrow-Owen, H. Cui, J. Alexander-Webber, F. Gu, X. Wang, T.-C. Wu, M. Zhuge, C. Williams, P. Wang, A. V. Zayats, W. Cai, L. Dai, S. Hofmann, M. Overend, L. Tong, Q. Yang, Z. Sun, T. Hasan, *Science (80-)* **2019**, *365*, 1017.
[14] Z. Wang, S. Yi, A. Chen, M. Zhou, T. S. Luk, A. James, J. Nogan, W. Ross, G. Joe, A. Shahsafi, K. X. Wang, M. A. Kats, Z. Yu, *Nat. Commun.* **2019**, *10*, 1020.
[15] B. Redding, M. Alam, M. Seifert, H. Cao, *Optica* **2014**, *1*, 175.
[16] W. Hartmann, P. Varytis, H. Gehring, N. Walter, F. Beutel, K. Busch, W. Pernice, *Nano Lett.* **2020**, *20*, 2625.
[17] B. Redding, S. F. Liew, R. Sarma, H. Cao, *Nat. Photonics* **2013**, *7*, 746.
[18] W. Hadibrata, H. Noh, H. Wei, S. Krishnaswamy, K. Aydin, *Laser Photonics Rev.* **2021**, *15*, 2000556.
[19] A. Li, Y. Fainman, *Nat. Commun.* **2021**, *12*, 2704.
[20] B. Redding, S. Fatt Liew, Y. Bromberg, R. Sarma, H. Cao, *Optica* **2016**, *3*, 956.
[21] Z. Zhang, Y. Li, Y. Wang, Z. Yu, X. Sun, H. K. Tsang, *Laser Photonics Rev.* **2021**, *15*, 2100039.
[22] L. Gao, Y. Qu, L. Wang, Z. Yu, *Nanophotonics* **2022**, *11*, 2507.
[23] A. Li, C. Yao, J. Xia, H. Wang, Q. Cheng, R. Penty, Y. Fainman, S. Pan, *Light: Sci. Appl.* **2022**, *11*, 174.
[24] J. Zhang, Z. Cheng, J. Dong, X. Zhang, *Optica* **2022**, *9*, 517.
[25] S. Yuan, D. Naveh, K. Watanabe, T. Taniguchi, F. Xia, *Nat. Photonics* **2021**, *15*, 601.
[26] L. Zhang, M. Zhang, T. Chen, D. Liu, S. Hong, D. Dai, *Opto-Electron. Adv.* **2017**, *5*, 210100.
[27] C. Sun, Z. Chen, Y. Yin, Y. Ye, Y. Luo, H. Ma, J. Jian, Y. Shi, C. Zhong, D. Zhang, H. Lin, L. Li, *ACS Photonics* **2022**, *9*, 2973.
[28] Y. Zhi, X.-C. Yu, Q. Gong, L. Yang, Y.-F. Xiao, *Adv. Mater.* **2017**, *29*, 1604920.
[29] L. He, Ş. K. Özdemir, L. Yang, *Laser Photonics Rev.* **2013**, *7*, 60.
[30] N. L. B. Sayson, T. Bi, V. Ng, H. Pham, L. S. Trainor, H. G. L. Schwefel, S. Coen, M. Erkintalo, S. G. Murdoch, *Nat. Photonics* **2019**, *13*, 701.
[31] B. Cerjan, N. J. Halas, *ACS Photonics* **2018**, *6*, 79.
[32] Y. Zhang, Y. He, Q. Zhu, X. Guo, C. Qiu, Y. Su, R. Soref, *Opt. Lett.* **2018**, *43*, 4518.
[33] J. Liao, L. Yang, *Light: Sci. Appl.* **2021**, *10*, 32.